# Device-Free Pedestrian Tracking Using Low-Cost Ultra-Wideband Devices

Chenglong Li, Emmeric Tanghe, *Member, IEEE,* Luc Martens, *Member, IEEE,*
Jac Romme, Gaurav Singh, Eli De Poorter, and Wout Joseph, *Senior Member, IEEE*

*Abstract*—**Ultra-wideband (UWB) attracts extensive attention for the Internet-of-Things applications, especially the fine-grained location-based services. Rather than active tracking, this paper explores the UWB-based device-free pedestrian tracking problem. Concerning the challenges of fine-grained passive tracking for the low-cost commodity UWB devices, we propose a variance-based temporary-spatial (VATS) mapping algorithm, which relieves the background interference from the perspective of the Bayesian framework. Moreover, a particle filter algorithm has been designed to track the position likelihood changing and to avoid likelihood ambiguity. Experimental results show that the proposed VATS mapping algorithm achieves 50-th and 90-th percentile errors 0.156 m and 0.272 m, respectively, which is promising for practical applications.**

*Index Terms*—**Indoor localization, ultra-wideband (UWB), passive tracking, channel impulse response (CIR), radar.**

## I. INTRODUCTION

**R**ADIO frequency-based device-free (passive) positioning and sensing has attracted increasing interest in recent years, especially when the physical-layer information (channel response) is available for the low-cost commercial radio devices [1]–[3], such as WiFi, radio frequency identification (RFID), ultra-wideband (UWB), etc. Without the requirement of visibility or attaching sensors to the users, passive RF-based sensing is appreciated for the various applications considering the feasibility, security, and privacy issues. UWB technique, resulting from its high time-domain resolution, is widely utilized for accurate ranging and positioning, even in a cluttered industrial environment [4], [5]. Besides active localization, passive sensing is also popular in the field of smart Internet-of-Things (IoT), such as person tracking [6], [7], through-the-wall vital sign detection [8], [9], crowd counting [10], gesture recognition [11], etc. However, most UWB passive sensing researches utilize the vector network analyzer (VNA) setup or other dedicated devices (quasi-perfect synchronization, high sampling rate, etc.), which limits the extensive deployment for the practical use cases. Recently, [3] proposed to adopt the low-cost commercial off-the-shelf (COTS) UWB modules for passive human tracking and achieved decimeter-level accuracy.

In this paper, we also focus on device-free human tracking based on COTS UWB devices. For RF-based pedestrian tracking, an intuitive idea is to estimate the reflected time-of-flight (ToF) from the moving person first, then pinpoint the person's location via the intersection of the multiple ellipses when the reflected ToFs of multiple pairs of transceivers are available [3], [12]. However, in this case, it is not easy to mitigate the impact of background for the COTS devices, which will be explained in detail in Section II. Furthermore, radio tomographic imaging (RTI) is another popular technique for device-free localization by imaging the attenuation caused by the pedestrian [13], [14]. However, the accuracy depends on a large density of anchors (transmission links). Different from the approaches mentioned above, we propose a novel variance-based temporary-spatial (VATS) mapping algorithm that converts the variances of channel impulse responses (CIR) from the delay domain to the spatial domain (i.e., Cartesian coordinates within the targeted area). The experimental validation shows that the proposed method is advantageous to background mitigation and achieves promising accuracy.

## II. PRACTICAL CONCERNS FOR COTS UWB DEVICES

Due to the advantage of large bandwidth, UWB can depicts the multipath components (MPCs) with fine granularity in the delay domain. The CIR $h(\tau)$ in case of a single moving person can be given by (in equivalent baseband notation),

$$h(\tau) = \sum_{i \in \mathcal{B}} \alpha_i \delta(\tau - \tau_i) + \sum_{j \in \mathcal{P}} \alpha_j \delta(\tau - \tau_j) + \mathbf{n}, \quad (1)$$

where $\mathcal{B}$ and $\mathcal{P}$ represent the MPCs from the background (including the direct link and reflection/scattering from surroundings) and the moving person, respectively. $\alpha_{(\cdot)}$ denotes the complex gain of the MPCs. Note that $\tau$ and $\tau_{(\cdot)}$ are not defined as the real ToFs but the delays relative to the direct link hereinafter. $\mathbf{n}$ is the measurement noise. To estimate the delay from the target $\tau_j$ $(j \in \mathcal{P})$, we need to mitigate the impact of background. However, the background mitigation is not easy for the COTS UWB devices, e.g., DecaWave DWM1000 [15].

The chipping frequency of the DWM1000 is 499.2 MHz, so the time resolution of the CIR sample is 1.0016 ns. As shown in Fig. 1, the blue dots are a single CIR measurement of which the 4-th sample represents the line-of-sight (LoS) delay identified by DWM1000 via the leading edge (LDE) algorithm [15]. Because the CIR resolution is about 1 ns (i.e., 30 cm in the spatial domain), it does not always capture the fine-grained spatial variation of the moving person. As shown in Fig. 1, the CIR samples may step across the real

delay of the path reflected off the moving person (vertical red line). For DWM1000 modules, they are triggered by the local clocks. The CIRs between any two UWB nodes were sampled at slightly different times. We can accumulate the CIRs within a short duration and align the CIRs around the reported LoS CIR bin [3], [12], [16], as the grey dots presented in Fig. 1 with 50 consecutive CIR measurements. We conduct the same accumulation technique for both background (no person moving) and dynamic scenarios. Two examples of the accumulated CIRs are presented in Figs. 2 and 3. Three conclusions can be drawn from these figures.

- When the delay relative to the LoS link is small, namely the person close to the transceiver link, we can observe a clear CIR peak caused by the human body reflection or scattering. However, when the delay enlarges, this peak becomes very small (close to the background CIR), which challenges background mitigation from CIR directly.
- The pedestrian not only causes the CIR variations around the real delay but also affects the CIR segment following, which was observed in [16] as well.
- The LoS peak's amplitude is unstable. Because the accumulated CIR is centered around the LoS bin identified by the LDE algorithm, the LoS peak's amplitude also fluctuates as a result of LDE's errors.

So (1) in case of COTS UWB devices can be adapted to

$$h(\tau) = \sum_{i \in \mathcal{B}} \alpha_i \delta(\tau - \tau_i) + \sum_{j \in \mathcal{P}} \alpha_j \delta(\tau - \tau_j) + \mathbf{n} \\ + \sum_{k \in \bigcup_0 \subseteq \mathcal{B}} \alpha_k \delta(\tau - \tau_k) + \sum_{l \in \mathcal{S} \subseteq \mathcal{B}} \alpha_l \delta(\tau - \tau_l), \quad (2)$$

where $\bigcup_0$ and $\mathcal{S}$ represent the fluctuation errors around the LoS bin and the following CIR segments with larger delays than the moving person, respectively. According to the remarks above, it is not easy to mitigate the background from the CIR directly especially when the relative delay is large (namely, the pedestrian moves far away from the transceiver link).

Fortunately, we observe that the CIR's amplitude around the real delay fluctuates greatly despite a large relative delay, as shown in Fig. 3, which means it is possible to use the variance within a short segment of the CIR series to identify the delay. Fig. 4 shows the variance of CIR in Fig. 3, in which a clear peak around the real delay has been observed. However, at the same time, the fluctuations at $\bigcup_0$ and $\mathcal{S}$ still exist as the green and orange ellipses in Fig. 4 indicate. To mitigate the impact of LoS fluctuations, [3] proposed to multiply a scaling factor $\beta$ (e.g., $\beta = 1.3$ as recommended in [3]) by the background variance, and then use the dynamic variance to subtract the scaled background variance. Then a variance-based LDE algorithm was designed to find the first bin having the variance difference larger than the threshold. In this case, the impact of the later CIR segment has also been canceled. But the scaling factor is related to the background environment, which needs refinement for different pairs of links or new scenarios to achieve satisfying accuracy. A bad selection of the factor will degrade the performance greatly. Instead of mitigating based on empirical scaling parameter, in [12], we proposed to input the background and dynamic variance series
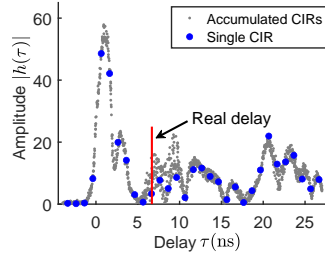


Fig. 1. Accumulated CIRs (50 measurements) versus single CIR.
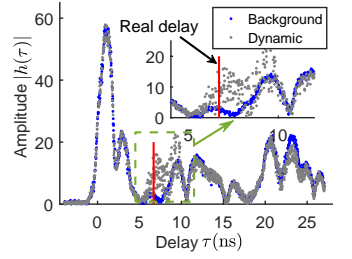


Fig. 2. Background and dynamic CIRs (real delay = 6.69 ns).
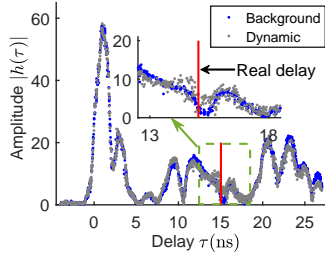


Fig. 3. Background and dynamic CIRs (real delay = 15.04 ns).
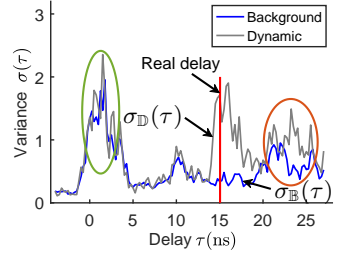


Fig. 4. Background and dynamic variances (real delay = 15.04 ns).

into a residual convolutional neural network (CNN) directly and learn the difference between the background and dynamic scenarios as a black box, which achieved better results than the variance-based LDE algorithm. However, deep learning (DL) model is expensive to implement on the low-cost hardware considering the feasibility and energy consumption [4].

## III. ALGORITHM DESIGN FOR DEVICE-FREE TRACKING

### A. Variance-based Temporary-Spatial Mapping

As mentioned in Section II, the variance is a more robust metric than the CIR for passive tracking. However, it still suffers from the impact of fluctuations around LoS ($\bigcup_0$) and the following CIR segment ($\mathcal{S}$). To handle this issue, we propose the VATS mapping algorithm, which converts the variance differences between background and dynamic CIR variances from delay domain to spatial domain (i.e., Cartesian coordinates within the targeted area). Define $\sigma_{\mathbb{B}}(\boldsymbol{\tau}_{ij})$ and $\sigma_{\mathbb{D}}(\boldsymbol{\tau}_{ij})$ as the variance series of the $(i, j)$-th pair of link for the background and dynamic scenarios, respectively, as shown in Fig. 4. The variance difference is given by $\Delta\sigma(\boldsymbol{\tau}_{ij}) = \sigma_{\mathbb{D}}(\boldsymbol{\tau}_{ij}) - \sigma_{\mathbb{B}}(\boldsymbol{\tau}_{ij})$, where $\boldsymbol{\tau}_{ij}$ represents the set of possible delays of the variance profile, i.e., the $x$-axis in Fig. 4. So the VATS mapping $\mathcal{M}$ can be expressed as,

$$\Delta\sigma\left(\mathbf{P}_{\mathrm{P}}\right) \xleftarrow{\mathcal{M}} \Delta\sigma\left(\boldsymbol{\tau}_{ij}^{(\mathrm{P})}\right) = \Delta\sigma\left(\boldsymbol{d}_{ij}^{(\mathrm{P})}/c\right), (i \neq j), \quad (3)$$

where $c$ is the speed of light. $\boldsymbol{d}_{ij}^{(\mathrm{P})}$ represents the reflected path length difference relative to the $(i, j)$-th direct link, given by,

$$\boldsymbol{d}_{ij}^{(\mathrm{P})} = \left\|\mathbf{P}_{\mathrm{P}} - \mathbf{P}_{\mathrm{Tx}}^{(i)}\right\| + \left\|\mathbf{P}_{\mathrm{P}} - \mathbf{P}_{\mathrm{Rx}}^{(j)}\right\| - \left\|\mathbf{P}_{\mathrm{Tx}}^{(i)} - \mathbf{P}_{\mathrm{Rx}}^{(j)}\right\|,$$

where $\mathbf{P}_{\mathrm{P}}$, $\mathbf{P}_{\mathrm{Tx}}$, and $\mathbf{P}_{\mathrm{Rx}}$ are the Cartesian coordinates of the pedestrian, transmitter, and receiver, respectively. $\|\cdot\|$ denote the $l_2$-norm operator. In this way, we build a mapping between the variance and pedestrian's location. For the variance calculation, we refer to the variance filtering method proposed

by [3], which is easily-implemented and efficient. We omit the detailed description in this paper due to the limited space. The details can be found in [3].

**Remark.** *After operating VATS mapping, the candidate locations of the moving person are a set of ellipses focusing on the UWB transceiver, as shown in Fig. 5(a). When increasing the number of UWB node $\mathcal{N}$, only the variance around the pedestrian's position will be enhanced by the most times, i.e., $\binom{\mathcal{N}}{2}$. Note that we assume that each UWB node acts as both the transmitter and receiver. To this end, we can pinpoint the pedestrian's position via identifying the maximum of the augmented variance hologram, as shown in Figs. 5(b)-(c).*

The above pedestrian passive tracking problem can be explained from the perspective of Bayesian framework. We can normalize $\Delta\sigma(\tau)$ via dividing $\int \Delta\sigma(\tau)\mathrm{d}\tau$. The normalized variance difference can be regarded as the likelihood at a certain delay, labeled as $f(\Delta\sigma\,|\,\tau)$. So the goal of positioning is to obtain the posterior distribution of $\mathbf{P}_\mathrm{P}$ given the variance difference of $\mathcal{N}$ UWB nodes, namely $f\left(\mathbf{P}_\mathrm{P}\,|\,\Delta\sigma_1,\cdots,\Delta\sigma_{\binom{\mathcal{N}}{2}}\right)$. With the help of (3), the posterior distribution becomes

$$f\left(\mathbf{P}_\mathrm{P}\,|\,\Delta\sigma_1,\cdots,\Delta\sigma_{\binom{\mathcal{N}}{2}}\right) \propto f(\mathbf{P}_\mathrm{P}) \prod_{i=1}^{\binom{\mathcal{N}}{2}} f\left(\Delta\sigma_i\,|\,\tau\right), \quad (4)$$

where $f(\mathbf{P}_\mathrm{P})$ is the prior distribution of $\mathbf{P}_\mathrm{P}$. So, the position of the pedestrian can be estimated via, e.g., maximum a posterior (MAP) estimator. We assume $f(\mathbf{P}_\mathrm{P})$ follows an uniform distribution, so the MAP becomes a maximum likelihood (ML) estimator, given by,

$$\hat{\mathbf{P}}_\mathrm{P} = \arg\max_{\mathbf{P}_\mathrm{P}} \prod_{i=1}^{\binom{\mathcal{N}}{2}} f\left(\Delta\sigma_i\,|\,\tau\right) \triangleq \arg\max_{\mathbf{P}_\mathrm{P}} \prod_{i=1}^{\binom{\mathcal{N}}{2}} \Delta\sigma_i(\tau). \quad (5)$$

### B. Particle Filter-based Pedestrian Tracking

According to (5), the pedestrian's location is pinpointed via the maximal likelihood. However, we also observe that there may exist some ambiguity locations with local maximal likelihood (the yellow regions), even larger than the likelihood around the the pedestrian's position, as shown in Fig. 5(d). To tackle this ambiguity problem, instead of simply searching for the location with the maximal likelihood, we design a particle filter (PF) algorithm to track the likelihood changing. The state of the PF is the 2-D coordinates $\mathbf{P}_\mathrm{P}$ and velocity $\mathbf{v}_\mathrm{P}$ of the moving person, which is updated via the movement model given as follows,

$$\begin{bmatrix} \mathbf{P}_\mathrm{P}^{(t+1)} \\ \mathbf{v}_\mathrm{P}^{(t+1)} \end{bmatrix} = \begin{bmatrix} \mathbf{I}_2 & \Delta t \cdot \mathbf{I}_2 \\ \mathbf{0} & \mathbf{I}_2 \end{bmatrix} \begin{bmatrix} \mathbf{P}_\mathrm{P}^{(t)} \\ \mathbf{v}_\mathrm{P}^{(t)} \end{bmatrix} + \begin{bmatrix} \Delta t \cdot \mathbf{1}_{2\times 1} \\ \mathbf{1}_{2\times 1} \end{bmatrix} n_v, \quad (6)$$

where $\Delta t$ is the time difference between timestamps $t$ and $t+1$. $n_v$ is the Gaussian error of velocity, of which the standard deviation is set as $0.3\mathrm{m/s}$. The updated particles are weighted via the likelihood difference compared with the maximal likelihood. The weight is calculated via

$$\hat{P}_w^{(i)} = \exp\left(\frac{1}{2\sigma_w^2}\left(\min_{1\le i\le K}\left\{P_w^{(i)}\right\} - P_w^{(i)}\right)\right),$$
$$P_w^{(i)} = \left(\mathbf{P}_{\max} - \Delta\sigma\left(\mathbf{P}_\mathrm{P}^{(i)}\right)\right)^2, \quad (7)$$
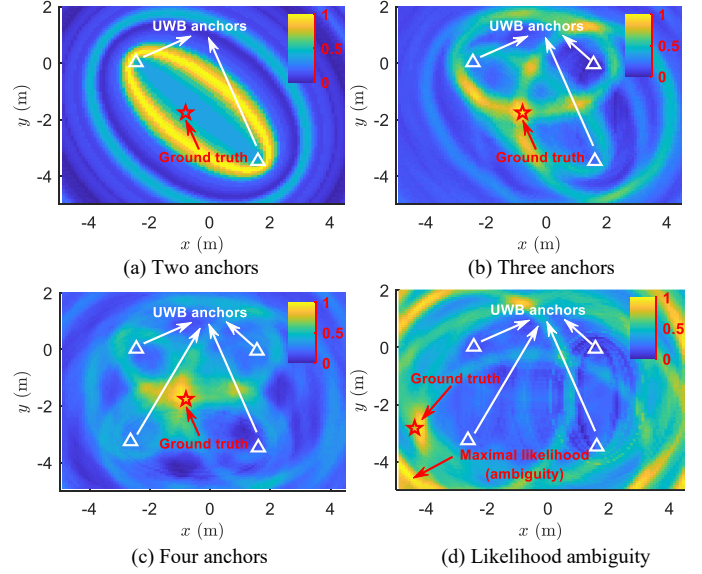


Fig. 5. (a)-(c) Holograms of the normalized positioning likelihood with different numbers of anchors. (d) Positioning likelihood ambiguity.

where $K$ is the number of particles. Because we normalize $\Delta\sigma(\mathbf{P}_\mathrm{P})$ to $[0,1]$, as the colorbar shown in Fig. 5, the maximal likelihood $\mathbf{P}_{\max} = 1$. The standard deviation $\sigma_w$ is set as $0.1$.

## IV. EXPERIMENT AND RESULTS

### A. Experiment

In this section, the proposed VATS mapping algorithm for the device-free pedestrian tracking will be evaluated through the experiment using COTS UWB devices. The corresponding measurement data is open-access in [17]. The explanation of the dataset will be briefly introduced below. The details can be found in [3], [17]. Four DWM1000 UWB anchors (about 1.2 m in height) were deployed in an indoor laboratory environment. The size of the targeted area is about $8\mathrm{m} \times 6\mathrm{m}$. The UWB anchors sent messages to each other with an average frequency of 188 Hz. The adopted frequency is 3993.6 MHz, bandwidth 900 MHz, and pulse repetition frequency 16 MHz. The ground truth of the moving trajectory was obtained via the motion capture (MoCap) system with millimeter-level accuracy.

Note that the experiment only considered single-person tracking, but the proposed VATS mapping algorithm can be easily adapted to multi-person tracking via regarding the posterior distribution in (4) as a joint distribution for multiple targets and adopting a multi-target particle filter algorithm.

### B. Performance Evaluation

Figs. 6(a)-(b) show the tracking trajectory based on the proposed VATS mapping algorithm using three anchors and four anchors, respectively. The tracking errors are defined as the distance between the estimated position and ground truth, which has been presented along the estimated trajectory. We can see that the proposed algorithm achieves very high tracking precision even with only three anchors (with mean errors 0.238 m). For the four anchors case, the mean tracking accuracy reaches an excellent result of 0.169 m despite a very
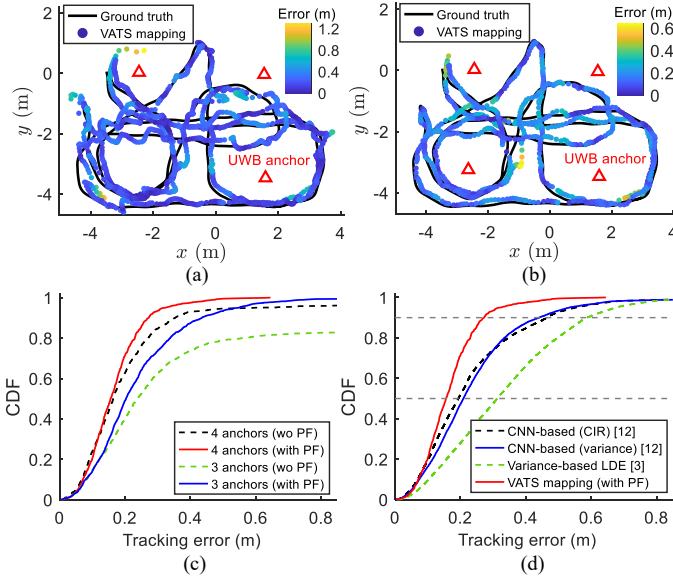
Fig. 6. (a) Tracking accuracy of three anchors. (b) Tracking accuracy of four anchors. (c) CDF of the tracking errors (with three or four anchors): the effectiveness of PF. (d) Comparison with SOTA methods under four anchors.

TABLE I
COMPARISON OF THE STATISTICAL TRACKING ERRORS WITH FOUR ANCHORS IN METER.

| Methods | 50-th | 90-th | Improvement | DL |
|---|---|---|---|---|
| **CNN (CIR)** [12] | 0.194 | 0.465 | 19.6%-41.5% | Yes |
| **CNN (variance)** [12] | 0.209 | 0.440 | 25.4%-38.2% | Yes |
| **Variance-based LDE** [3] | 0.312 | 0.588 | 50.0%-53.7% | No |
| **VATS mapping** | **0.156** | **0.272** | / | No |

limited number of outliers (with distance errors larger than 0.5 m). In Fig. 6(c), we investigate the impact of with (solid lines) or without (wo, dash lines) PF tracker under the VATS mapping algorithm via the cumulative distribution functions (CDF) of tracking errors. The results validate the effectiveness of PF tracking which avoids the large errors resulting from likelihood ambiguity.

Furthermore, we compare the proposed VATS mapping algorithm with different state-of-the-art (SOTA) methods proposed recently [3], [12] in case of four UWB anchors. Because the methods (CIR and variance) in [12] are based on CNN training. For the comparison, we have used the first 66.7% trajectory data as the training set and regarded the prediction performance on the remaining trajectory as the tracking accuracy of the models. As shown in Fig. 6(d), the proposed method (no DL needed) has achieved the best tracking accuracy, while the variance-based LDE is worse than the CIR- and variance-based CNN models. We summarize the percentile errors (i.e., 50-th and 90-th) in Table I. The proposed method outperforms the others achieving 50-th percentile errors 0.156 m and 90-th percentile errors 0.272 m (more than 19.6% improvement).

## V. CONCLUSION

In this paper, we have investigated device-free human tracking based on low-cost UWB devices. A novel VATS mapping method, together with a particle filter algorithm,

has been proposed for background mitigation and fine-grained pedestrian tracking. According to the experimental evaluation, the proposed method achieves excellent results with 50-th and 90-th percentile errors 0.156 m and 0.272 m, respectively, which has more than 19.6% improvement compared with the available SOTA methods. In a nutshell, the proposed algorithm is advantageous to high accuracy and feasible implementation (no machine/deep learning involved) and promising for practical applications. Future works will consist of quantifying the impact of anchors' number on the likelihood ambiguity and accuracy, multi-target tracking in a more cluttered environment, and distinguishing pedestrian and moving robots.

## REFERENCES

[1] Z. Fu, J. Xu, Z. Zhu, A. X. Liu, and X. Sun, "Writing in the air with WiFi signals for virtual reality devices," *IEEE Transactions on Mobile Computing*, vol. 18, no. 2, pp. 473–484, Feb 2019.
[2] C. Li, E. Tanghe, P. Suanet, D. Plets, J. Hoebeke, E. De Poorter, and W. Joseph, "ReLoc 2.0: UHF-RFID relative localization for drone-based inventory management," *IEEE Transactions on Instrumentation and Measurement*, vol. 70, pp. 1–13, Mar 2021.
[3] A. Ledergerber and R. D'Andrea, "A multi-static radar network with ultra-wideband radio-equipped devices," *Sensors*, vol. 20, no. 6, pp. 1–20, Mar 2020.
[4] J. Fontaine, M. Ridolfi, B. Van Herbruggen, A. Shahid, and E. De Poorter, "Edge inference for UWB ranging error correction using autoencoders," *IEEE Access*, vol. 8, pp. 139 143–139 155, Jul 2020.
[5] L. Barbieri, M. Brambilla, A. Trabattoni, S. Mervic, and M. Nicoli, "UWB localization in a smart factory: Augmentation methods and experimental assessment," *IEEE Transactions on Instrumentation and Measurement*, vol. 70, pp. 1–18, Apr 2021.
[6] S. Chang, R. Sharan, M. Wolf, N. Mitsumoto, and J. W. Burdick, "UWB radar-based human target tracking," in *IEEE Radar Conference*, May 2009, pp. 1–6.
[7] M. McCracken and N. Patwari, "Hidden markov estimation of bistatic range from cluttered ultra-wideband impulse responses," *IEEE Transactions on Mobile Computing*, vol. 13, no. 7, pp. 1509–1521, Jul 2014.
[8] J. Li, Z. Zeng, J. Sun, and F. Liu, "Through-wall detection of human being's movement by UWB radar," *IEEE Geoscience and Remote Sensing Letters*, vol. 9, no. 6, pp. 1079–1083, Nov 2012.
[9] X. Liang, H. Zhang, S. Ye, G. Fang, and T. Aaron Gulliver, "Improved denoising method for through-wall vital sign detection using UWB impulse radar," *Digital Signal Processing*, vol. 74, pp. 72–93, Mar 2018.
[10] J.-H. Choi, J.-E. Kim, and K.-T. Kim, "People counting using IR-UWB radar sensor in a wide area," *IEEE Internet of Things Journal*, vol. 8, no. 7, pp. 5806–5821, Apr 2021.
[11] B. Li, J. Yang, Y. Yang, C. Li, and Y. Zhang, "Sign language/gesture recognition based on cumulative distribution density features using UWB radar," *IEEE Transactions on Instrumentation and Measurement*, vol. 70, pp. 1–13, Jun 2021.
[12] C. Li, E. Tanghe, J. Fontaine, L. Martens, J. Romme, G. Singh, E. D. Poorter, and W. Joseph, "Multi-static UWB radar-based passive human tracking using COTS devices," *IEEE Antennas and Wireless Propagation Letters*, pp. 1–5, 2022.
[13] J. Wilson and N. Patwari, "Radio tomographic imaging with wireless networks," *IEEE Transactions on Mobile Computing*, vol. 9, no. 5, pp. 621–632, May 2010.
[14] K. Bregar, A. Hrovat, M. Mohorčič, and T. Javornik, "Self-calibrated UWB based device-free indoor localization and activity detection approach," in *European Conference on Networks and Communications*, Jun 2020, pp. 176–181.
[15] Decawave, "DW1000 User Manual," [Online]. Available: https://www.decawave.com/sites/default/files/resources/dw1000_user_manual_2.11.pdf, 2017.
[16] A. Moschevikin, E. Tsvetkov, A. Alekseev, and A. Sikora, "Investigations on passive channel impulse response of ultra wide band signals for monitoring and safety applications," in *International Symposium on Wireless Systems within the Conferences on Intelligent Data Acquisition and Advanced Computing Systems*, Sep 2016, pp. 97–104.
[17] A. Ledergerber, "Dataset accompanying paper 'A multi-static radar network with ultra-wideband radio-equipped devices'," [Open access]. Available: https://doi.org/10.3929/ethz-b-000397625, Feb 2020.